# Electric Field Visualization and Quantitative Analysis Based on Electroluminescence Effect Excited by High-Frequency Square Wave Voltage

Kai Wang, Donglei Dai, Chongxing Zhang, Ming Dong, *Member, IEEE*, and Ming Ren, *Member, IEEE*

***Abstract*—To achieve the visualization and quantitative analysis of electric fields for direct bond copper (DBC) substrate, the characteristics of square wave excitation electroluminescence (EL) are investigated to develop the electric field reversion model. Initially, the single photon counting technique and luminescence spectroscopy of EL devices are carried out to reveal the luminescence mechanism. Then, the reference fitting model is constructed for EL intensity and dimensionless electric field index using Gaussian process regression. Subsequently, finger electrodes are fabricated to investigate the electric field inversion procedure for quasi-uniform fields. Besides, considering the significant correlation between EL intensity and the electric field at both ends of EL powder, as well as the influence of strong light radiation on the measured luminescence at this time, the EL distribution is corrected based on the blind deconvolution algorithm. In addition, the electric field distribution is visually derived based on the reference inversion model. The goodness of linear fit between the electric field index at the center point of the electrodes and the applied voltage reached 98.85%. Finally, the above inversion method is experimentally validated on a double-sided DBC substrate, conclusively demonstrating its capability to effectively visualize anomalous electric field regions with high resolution.**

***Index Terms*—Direct bond copper (DBC) substrate, electric field inversion, electroluminescence (EL), insulation verification, power module.**

## I. INTRODUCTION

IN THE past decades years, medium-voltage wide-bandgap silicon carbide (SiC) power semiconductors have developed rapidly within the 10–15 kV range [1]. It aims to replace the traditional multilayer and multilevel integrated energy conversion systems with higher power density packaging, which is accompanied by the rapid developments of power module layout optimization and packaging innovations. Currently, the maximum voltage of a single SiC chip can reach 15 kV or even 30 kV benefiting from the progress of wide-bandgap semiconductor technology [2]. However, it meets the challenges of high voltage, frequency, switching speed, and temperature in the process of packaging such high-voltage chips. Among them, focusing on the packaging optimization of medium-voltage power modules, insulation reliability is the key factor for ensuring safe and reliable operation [6].

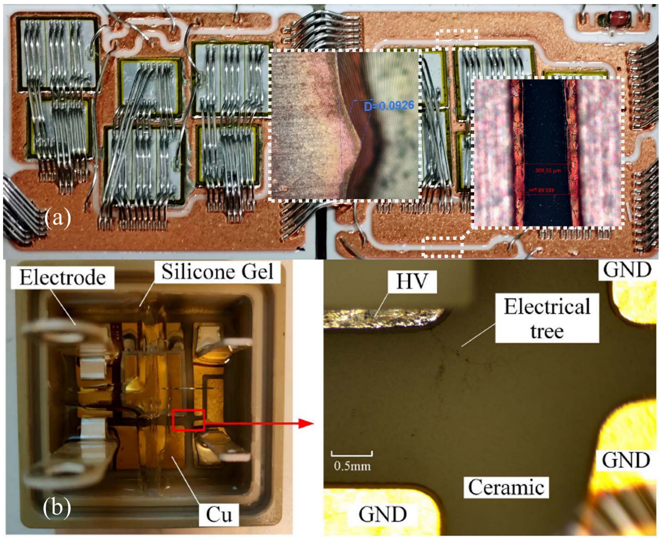

Fig. 1. (a) Diagrams of typical copper traces. (b) Electrical tree on the DBC ceramic [9].

Insulation failure of power modules generally develops from the electric field distortion areas due to the inappropriate layout design and limited manufacturing process level [7], [8], [9], as shown in Fig. 1(a). Besides, due to the influence of loop parasitic parameters, partial discharge (PD) appears at electric field distortion areas under the excitation of long-term ringing and voltage overshoot [6]. It develops into insulation failure under a high junction temperature environment quickly considering the aging of insulation materials and the enhancement of PD intensity [10]. As shown in Fig. 1(b), the electric tree is formed near the interface of the direct bond copper (DBC) substrate under the repetition rate square wave (SW) excitation [9]. Such PDs occurred inside the module but did not destroy the integrity of the module, however, it heavily weakened the insulation strength between the copper traces. In summary, it is essential to eliminate insulation problems caused by abnormal

Received 9 September 2024; revised 26 December 2024 and 3 March 2025; accepted 2 April 2025. Date of publication 10 April 2025; date of current version 26 May 2025. This work was supported by the National Key R&D Program of China “Remote monitoring and fault diagnosis technology for offshore wind power grid connected systems” under Grant 2023YFB2406900. Recommended for publication by Associate Editor Y. Zhang. *(Corresponding author: Ming Ren.)*

The authors are with the State Key Laboratory of Electrical Insulation and Power Equipment, Xi’an Jiaotong University, Xi’an 710049, China (e-mail: wangkai9370@stu.xjtu.edu.cn; daidonglei@stu.xjtu.edu.cn; zhang-cx@xjtu.edu.cn; dongming@xjtu.edu.cn; renming@xjtu.edu.cn).

Color versions of one or more figures in this article are available at https://doi.org/10.1109/TPEL.2025.3558960.

Digital Object Identifier 10.1109/TPEL.2025.3558960

electric fields from the perspective of power module insulation design. For this purpose, it is necessary to accurately evaluate and verify the electric field distribution among the copper traces [11], [12].

For packaging 10–20 kV SiC MOSFETS, increasing the isolation distance is a common approach [13], [14]. In addition, substrate stacking is an effective solution that reduces the electric field strength by stacking multiple substrates [15], [16]. Generally, the insulation integrity of the power modules based on the above manufacturing approaches is evaluated by the PD inception voltage (PDIV). However, the existing techniques for detecting PD s under repetitive SW excitation face issues such as low detection rates and poor spatial resolution in localizing discharge positions. Hence, it is difficult to achieve early localization of the abnormal electric fields within power module substrates, which is essential for further guiding the optimization of insulation design.

Finite element simulation is commonly used to visualize the quasi-static electric field distribution between copper traces in the layout design stage [15], [17]. Considering that the terminals are subjected to high-frequency SW voltages, the electric field distribution is developed based on the excitation of harmonic components in the frequency domain, which are further deduced by the inverse Fourier transform [18], [19]. However, such a simulation method is developed based on ideal models, which makes it difficult to simulate the electric field distribution for the scenes of the impact of material parameters on simulation results under actual working conditions, irregular edges formed by preparation process limitations, and microdefects formed during the encapsulation process. Besides, electric field probes have been widely used to measure the surface electric field distribution for the external insulation of high-voltage power equipment [20], [21]. However, such a method based on the induced charge effect has a certain influence on the original electric field distribution of the testing object. Besides, the spatial resolution of the measured electric field is affected by many factors such as the size and shape of the probe [22], [23], [24], [25]. In addition, focusing on the application condition of the DBC substrate excited withstanding high-frequency SW voltage, it is of great significance to achieve fast response electric field measurement. Recently, stimulus-responsive materials excited by an electric field, thermal stimulus, and photoinduced effect have been rapidly applied in the field of reactive fluorescent probes, optoelectronic displays, flexible electronics, and other fields [26], [27]. Among them, electroluminescent (EL) materials excite electrons to transition to high energy states under high electric fields, and then the electrons recombine with the impurity energy levels introduced by hole doping, releasing energy, and emitting light. It exhibits promising potential in the visualization verification of abnormal electric fields due to the high luminescence efficiency and rapid response to rapidly changing electric fields [28].

Hence, cooperating with the EL effect and imaging process techniques, an electric field inversion approach is developed in this study to achieve the visualization and quantitative evaluation of electric field distribution under arbitrary structures. Guo et al. [28] studied the electric field distribution on the surface of insulators under ac excitation based on the EL effect, which revealed the charge polarization mechanism of EL particles. For the visualization application of electric field distribution of the DBC substrate of the high-voltage power module, the output terminal and bonding copper traces within these modules are subjected to high-frequency SW voltage excitation. Notably, the electric field distribution of the copper traces under high-frequency SW excitation may be significantly different from that under traditional industrial frequency ac excitation [29]. Considering the influence of dielectric constant difference on electric field distribution under multiharmonic components, composite luminescent material films with different doping ratios were prepared, and the dielectric response was measured to evaluate the optimal doping ratio. Subsequently, the electric field distribution under different harmonic components is superimposed to obtain the finger-shaped electrode electric field distribution. In addition, according to the EL mechanism under ac excitation, it can be inferred that the charge polarization effect will be stronger under SW excitation. To verify this hypothesis, an EL device based on a flat electrode structure is prepared. The time-resolution luminescence response and integrated spectrum detection system are developed for the EL mechanism under SW excitation. It is worth noting that there exist triple junction areas in various irregular electrode structures. When coating the composite EL material, the physical process of PDs and EL in these areas under high-voltage SW excitation is still unclear. Therefore, the physical development processes of EL and PDs are clarified based on the optical inspection platform, with which the two conditions can be distinguished in spectral distribution by integrated spectrum.

In addition, existing studies on electric field inversion based on the EL effect typically assume a linear relationship between the externally applied voltage and the electric field. It realizes electric field inversion using the exponential relationship between the EL intensity and the applied voltage with flat electrodes. However, such an approach overlooks the strong nonlinear characteristics of the electric field and voltage interactions under different electrode configurations, resulting in lower accuracy and applicability of electric field inversion. Hence, based on the developed optical inspection platform, the fitting relationships between brightness (using an EL device) and the dimensionless electric field index are established based on Gaussian process regression (GPR). It is further applied to achieve the electric field inversion for other electrode structures. Moreover, in terms of visualizing electric field distribution, previous studies typically used images captured by DSLR cameras as inputs for electric field inversion models. However, the actual measured light intensity is represented by the superposition of the radiation effects of other luminescent regions and their own brightness, especially near the triple junction region. To achieve better inversion accuracy, the blind deconvolution algorithm is introduced to solve the point spread function (PSF) and actual EL distribution of finger electrodes. Subsequently, the inversion of the electric field distribution of finger electrodes is deduced by the standard inversion model. Then the accuracy of the inversion results is verified by evaluating the linear fitting of the inverted electric field in the central point.

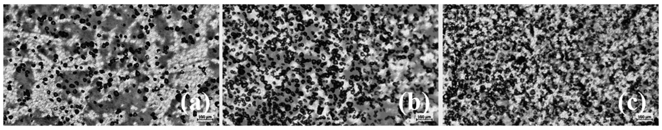

Fig. 2. Dispersions of EL particles with different mass fractions. (a) 8% wt. (b) 16% wt. (c) 24% wt.

## II. SPECIMEN DESIGN AND FABRICATION

### A. EL Composite Material and Coating Fabrication Processes

PDMS (Sylgard 184) is selected as the polymer matrix for EL powder ZnS:Cu (Shanghai Keyan Phosphor Technology, mean diameter size of ≈25 $\mu$m). Initially, components A and B are combined with proportions of 1:10, which is vigorously stirred for 10 min using a magnetic stirrer to ensure homogeneity. Then, EL powder is doped into the mixture according to a preset doping ratio and stirred for an additional 15 min to ensure thorough mixing. Subsequently, the mixture is placed in a vacuum oven and degassed for 20 min at a pressure of 0.02 MPa. During the coating phase, the processed mixture is evenly coated onto a 0.635-mm $Al_2O_3$ ceramic substrate using the scraper coating method, resulting in a uniform 200 $\mu$m thin layer. Finally, the coated sample is rapidly cured in a vacuum oven at 100 °C for 1 h. To ensure optimal distribution of EL particles on the ceramic substrate, we carefully observed particle dispersion under a microscope, focusing on samples with varying doping ratios (8%wt, 16%wt, 24%wt, and 32%wt) after coating and curing, as shown in Fig. 2.

### B. Broadband Dielectric Spectroscopy and Electrical Conductivity Analysis of Composite Coating Materials

Generally, SW voltage can be converted into a superposition of multiple harmonic components through Fourier transform. As mentioned in [18], the component with higher amplitudes has a stronger influence on the electric field's transient state. Equivalently, the components with larger amplitudes are significantly affected by the dielectric constant and conductivity. Therefore, it is necessary to evaluate the dielectric properties of composite silicone gels doped with EL powders. For this purpose, Novocontrol CONCEPT 43 is used to measure the dielectric properties of the pure PDMS and the composite ones, as shown in Fig. 3. The measured frequency ranged from 0.1 Hz to 10 kHz and the temperature was fixed at 25 °C. The test voltage was set to 400 $V_{AC}$. It can be found that the dielectric constants of each sample decrease as the frequency escalates, which is independent of the filler and mainly determined by the polymer matrix. Besides, as the doping ratio of luminescent particles increases, the dielectric constant of the composite material increases, which is attributed to the inherent dielectric response of luminescent particles and the contribution of interface effects related to Maxwell Wager Sillars contribution, including space charge accumulation [30]. As shown in Fig. 3(b), the dielectric loss also increases with the increase of filler content, mainly based on interface contribution, and these values are compatible with the capacitance effect required for EL applications, especially when operating in the frequency range above 1 kHz. Hence, balancing the luminescence brightness and dielectric properties, the doping ratio of 16%wt is selected as the optimal particle content.

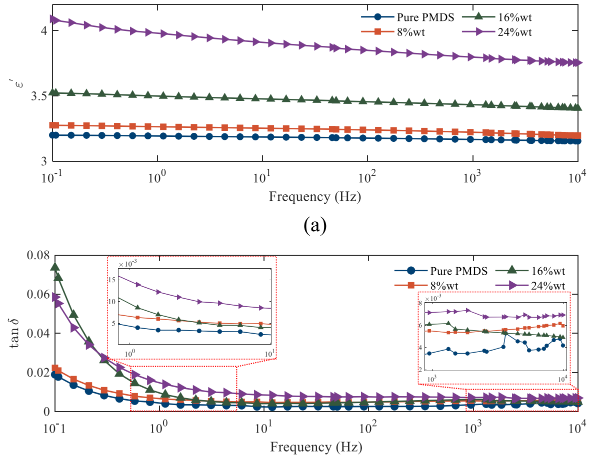

(a)

(b)

Fig. 3. (a) Dielectric constant and (b) dielectric loss of PDMS/ZnS:Cu films with different doping ratios of ZnS:Cu.

### C. Preparation of EL Device

It aims to visualize and quantify the surface electric field distribution of the DBC substrate based on the high-field EL effect in this study. Considering the investigation of voltage polarity, frequency, and voltage amplitude dependence of EL under SW excitation, it can better guide us to select appropriate image features and establish the corresponding electric field inversion model. Besides, there exists a typical triple-junction structure for the DBC substrate, where the electric field distribution among the copper traces is not uniform. Therefore, it is necessary to establish a reference inversion model for electric field inversion to apply to various insulating structures. For this purpose, we prepared an EL device with a planar electrode structure, as shown in Fig. 4(a). The device can obtain an electric field sufficient to cause luminescence at a lower external voltage, thereby flexibly investigating the EL characteristics under different voltage parameters. Furthermore, the EL device in this study was fabricated by sequentially screen-printing a luminescent layer (a mixture of ZnS:Cu and PDMS), an insulating layer (BaTiO3), and a lower electrode layer (conductive silver paste) onto a polyethylene terephthalate substrate coated with indium tin oxide (ITO). As shown in Fig. 4(b), the ITO-coated substrate was initially subjected to a drying pretreatment in an oven at 90 °C for 30 min. Then, the composite luminescent material was screen-printed onto the ITO substrate and cured in an oven at 90 °C for another 30 min. Subsequently, three layers of commercial $BaTiO_3$ slurry dielectric layer were applied onto the phosphor layer and cured for 10, 10, and 40 min, respectively. Finally, a conductive silver paste layer was screen-printed onto the insulation layer and dried at 120 °C for 40 min. Furthermore, a signal generator and power amplifier are employed to obtain the SW voltage with an adjustable peak-to-peak value of 200 V.

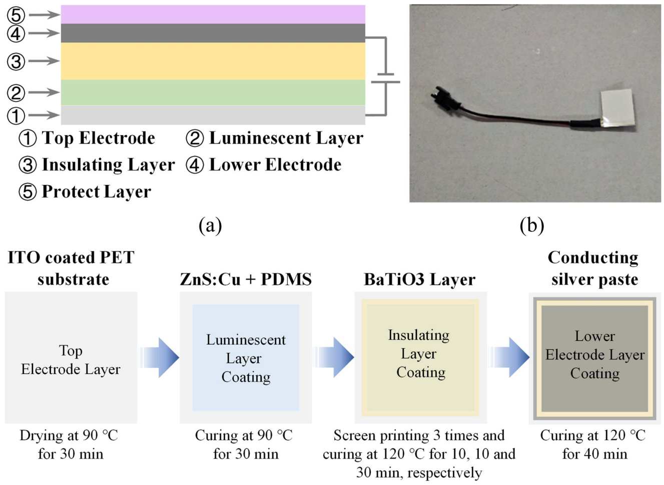

Fig. 4. (a) Structure EL device. (b) Schematic diagram of the fabrication of the EL device.

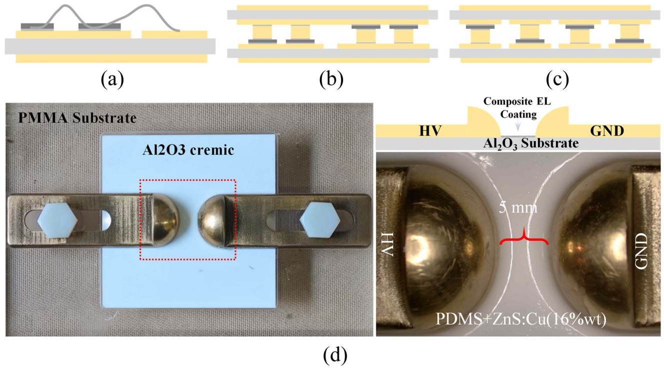

Fig. 5. Schematic diagram of the cross-section of the power module packaging structure. (a) 2-D packaging. (b) and (c) 3-D packaging [31], [32]. (d) Schematic of the fabricated finger electrodes.

## D. Double-Finger Electrode

The typical packaging structure of the power modules applying 2-D and 3-D packaging is shown in Fig. 5(a)–(c), which features a three-junction electric field distortion area that is created by the ceramic substrate, insulating encapsulation material, and the perimeter of the high-voltage copper-clad zone on a single DBC substrate. Such distortion region is a critical area to consider during the design and manufacturing process as it can impact the performance and reliability of the module. To explore the feasibility of using EL composite materials for visualizing electric field distribution, the electrode structure as shown in Fig. 5(d) was fabricated. Of which, a polymethyl methacrylate (PMMA) substrate is prepared to fix the $Al_2O_3$ ceramic substrate and the electrodes. Hence, a precise groove, measuring 50×50×2 mm, is milled in the central area of the PMMA base, serving as a receptacle for the alumina ceramic substrate. Besides, two electrode placement grooves (with a depth of 1 mm) are symmetrically milled on either side of the central groove. Subsequently, the finger electrodes are pressed tightly onto the ceramic substrate using PMMA screws with a spacing of 5 mm (with no obvious gaps at the electrode edges). Then, the composite EL slurry is uniformly coated on the ceramic substrate using a small silicone spatula. Then the sample is placed in a vacuum oven for degassing at a pressure of 0.02 MPa for 30 min and then cured at 90 °C for 40 min.

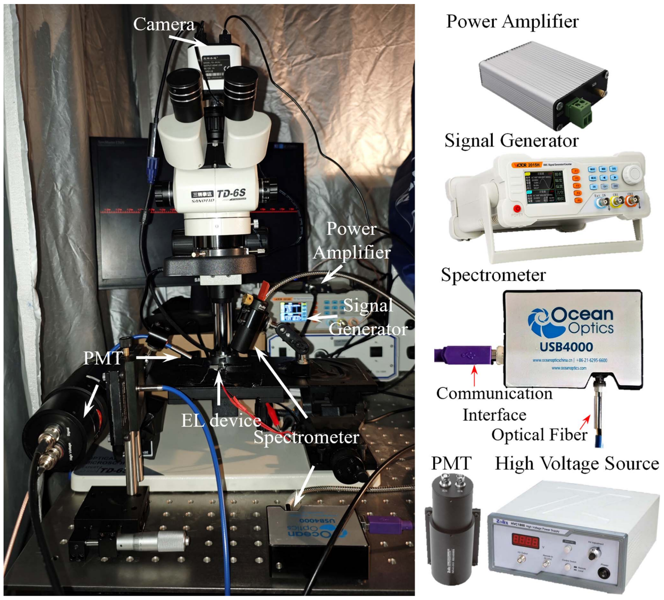

Fig. 6. Optical measurement platform.

## III. Dielectric Properties and Luminescence Characteristics of EL Composites

### A. Dependence Characteristics of Electroluminescence on SW Voltage Parameters

The optical measurement platform is set up in a dark room, as shown in Fig. 6. It contains a photomultiplier tube (PMTH-S1-CR131A, equipped with a high-voltage power supply Zolix HVC1800) to obtain the time-resolution response of the luminescence. Considering the damage to the photomultiplier tube (PMT) window cathode caused by the strong light generated by the large EL area, a multicore quartz fiber and a fiber-optic focusing detector were selected as a backup. Meanwhile, the high-voltage power supply is used to adjust the PMT output gain with various applied voltages. Furthermore, a spectrometer (Ocean Optics USB 4000, sensitive to the spectral range of 200–900 nm) is applied to measure the integrated spectrum of the EL emission. In addition, a stereo microscope equipped with a DSLR camera was used to capture long-exposure images of the EL device.

The photoresponse curves of EL under different polarity SW voltages are shown in Fig. 7, where the voltage frequency is set at 1 kHz, with a peak-to-peak value of 27 V and a duty cycle of 50%. Besides, the slew rates (SR) (measured at the 10%–90% voltage threshold on the rising edge) of each SW voltage are 902 mV/$\mu$s, 906 mV/$\mu$s, and 907 mV/$\mu$s, respectively. It can be observed that luminescence occurs during the switch transition process, where the luminescent intensity at the falling edge is slightly higher than that at the rising edge. The light response intensities at the rising and falling edges are recorded as 0.49 V,

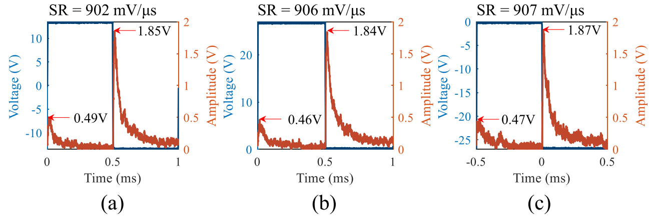

Fig. 7. PMT response under different polarity square wave excitations. (a) Bipolar. (b) Positive. (c) Negative polarity.

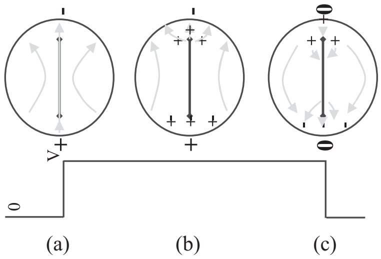

Fig. 8. Recombination process of electrons and holes inside luminescent particles under SW excitation.

0.46 V, and 0.47 V, and 1.85 V, 1.84 V, and 1.87 V, respectively. It demonstrates that the EL intensity is independent of the polarity of the applied voltage. It can be attributed to the process shown in Fig. 8(a)–(c). Previous studies have demonstrated the formation of linear $Cu_xS$ conductive phases during the preparation of ZnS doped with Cu. Upon the instantaneous application of an electric field, the electric field on the conductive wire undergoes distortion within its relaxation time, as exemplified in Fig. 8(b). Besides, the luminescent transition in ZnS occurs when free electrons in the conduction band fall into the excited activator center, thus the light emission occurs exclusively when electrons migrate to regions trapping holes. Meanwhile, the luminescence will be quenched when holes are injected into the area containing trapped electrons. Owing to the swifter migration speed of electrons, the built-in electric field consists primarily of hole traps situated near the positive electrode, as shown in Fig. 8(c). When the polarization field diminishes the field strength at the positive emitter, the current ceases to flow, and the potential barrier widens, preventing further emission. As the electric field returns to zero, the polarized electric field prompts the emission of electrons from the same location as the hole emission, leading to the generation of photons. Moreover, electrons recombine with trapped holes at the opposing end, producing light.

To explore the correlation between EL intensity and voltage at a fixed frequency, the integrated spectral curves of EL device excited by positive SW voltage with peak-to-peak voltages from 45 to 66 V are captured as shown in Fig. 9(a), which has an approximate characteristic peak of 495.21 nm. Following the previous research, the time-integrated brightness is most accurately described as [33]

$$L = Ae^{-(B/V)} \tag{1}$$

where $B$ indicates the concentration of the electric field at the barriers of the microcrystals of the electroluminophor [33]. Hence, the integrated light intensity at 495.21 nm satisfies formula (1) with a goodness of fit of 99.94%, as shown in Fig. 9(b). Similarly, the parametric fitting was performed on the trend of characteristic peaks with increasing voltage for the other two polarities, as shown in Table I, which further verifies the weak correlation between luminescence intensity and voltage polarity.

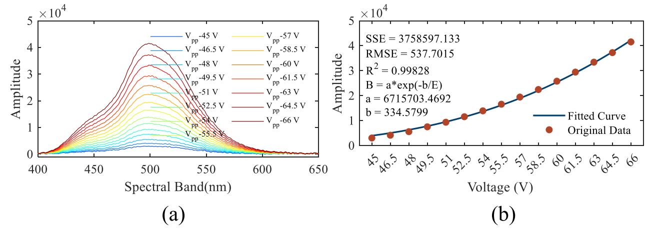

Fig. 9. (a) Integrated spectrum curves of EL at different peaks to peaks SW voltage. (b) Fitting curves of L–V for the peak values of the spectral characteristic.

TABLE I
FITTING COEFFICIENT OF (1) UNDER DIFFERENT POLARITY VOLTAGE EXCITATIONS

| Polarities | Parameter A | Parameter B |
|---|---|---|
| Bipolar | 3.14e6 | 331.12 |
| Positive | 3.09e6 | 321.31 |
| Negative | 2.93e6 | 326.26 |

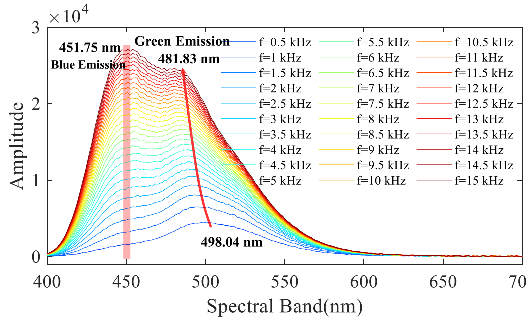

Fig. 10. Spectral distribution characteristics under different frequency unipolar SW excitation.

Besides, as shown in Fig. 10, the integral spectrum curves exhibit a blue shift in the main characteristic peak from 498.04 to 481.83 nm with an increase in frequency across the range of 0.5–15 kHz. Meanwhile, as the frequency increases, a secondary peak appears at 451.75 nm. It is considered that the luminescent center, $Cu_{2+}$, possesses two distinct luminescent energy levels, i.e., a deep acceptor level distant from the valence band, producing green luminescence, and a level closer to the valence band, emitting blue luminescence. Under low-frequency excitation, the holes present in the blue luminescent level are readily recombined with electrons originating from the green luminescent level, primarily due to vibrational relaxation [34]. Considering that the inversion of the spatial distribution of electric fields can be achieved by long exposure images, it is crucial to select appropriate feature band images under the SW excitation with a fixed frequency, which determines the quality of the mapping relationship between the EL intensity and the applied electric field.

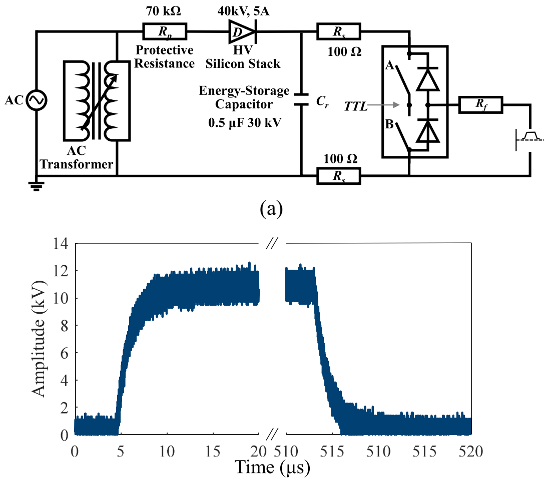

(a)

(b)

Fig. 11. Circuit diagram of high-voltage repetitive SW generator.

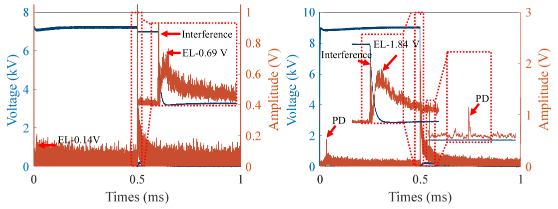

(a)

(b)

Fig. 12. Time resolution optical response for the finger electrodes.

### B. Spectral Distribution Characteristics of EL and Partial Discharge

To drive the EL of the composite coating under the finger electrode, a unipolar HV square pulse generator is developed based on an HV half-bridge module, as shown in Fig. 11(a). Of which, $R_p$ (70 kΩ) is the protective resistor, $C_r$ (0.5 $\mu$F, 30 kV) is the storage capacitor, and D denotes the HV silicon stack (40 kV, 5 A). $R_{s1}$ (100 Ω) and $R_{s2}$ (100 Ω) are the charging resistors at the rising and falling edges of the square pulse, respectively. Besides, a resistor Rf (5 Ω) is set to achieve the SRs of 4 ns/V, as shown in Fig. 11(b).

To determine the chronological order of EL and corona discharge events, the optical detection platform shown in Fig. 6 is used to capture the PMT response of both EL and PDs. As shown in Fig. 12(a), when the applied voltage is increased to 7 kV, PMT detects a significant EL light signal at the moment of voltage transition, where the intensity at the falling edge is much greater than that at the rising edge. Further increasing the voltage to 9 kV, the PD signals are captured by PMT near the voltage transition, as shown in Fig. 12(b). It indicates that for the double-finger electrode, EL precedes corona discharge, which can be attributed to the distortion of the conductive phase within the ZnS particles, resulting in high electric fields.

Furthermore, the spectral distribution that consists of EL and PDs is shown in Fig. 13 . The typical characteristic peaks of PDs appear in the range of 300– 400 nm, of which the second positive band of OH and $N_2$ was detected, and the strongest $N_2$ spectral line at 333 nm, peaking at 7259. Hence, such results illustrate that there exist significant differences between the physical processes of EL and PDs. Notably, it can be foreseen that the quantitative evaluation of electric field distribution for any electrode structures can be effectively achieved by developing the standard correlation between the luminescence intensity and the relative electric field strength.

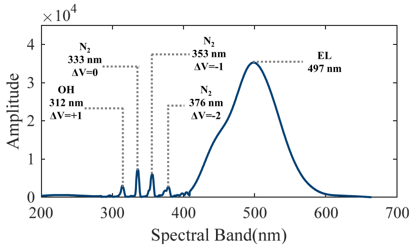

Fig. 13. Spectral distribution composed of PD and EL.

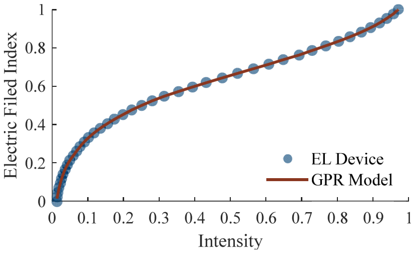

Fig. 14. Reference fitting model for the EL intensity and the normalized electric field index based on GPR.

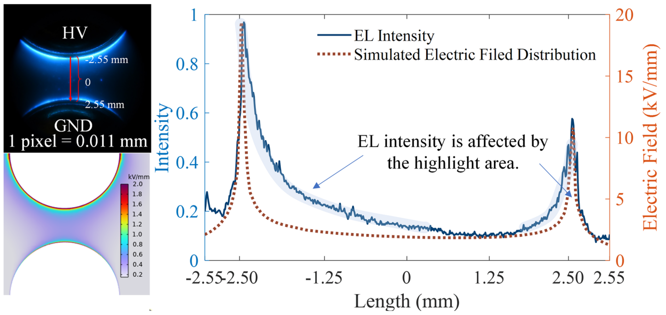

Fig. 15. Schematic diagram of comparison between EL distribution and the simulated electric field.

## IV. VISUALIZATION AND INVERSION OF ELECTRIC FIELD

### A. Nondimensional Quantitative Evaluation of Electric Field Distribution

To further obtain the spatial distribution of luminescence intensity and then achieve electrical inversion, a DSLR camera is used to capture long-exposure images with fixed parameters. Hence, the images of the EL device are captured excited by the SW voltage with a frequency of 1 kHz and increasing peak-to-peak values (from 30 to 50 V). Besides, a central 690×690 pixel area of the image is set as the Region of Interest (ROI). Then, the average color intensities for the green (G) channel of the image,

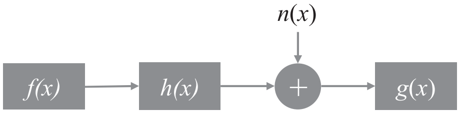

Fig. 16. Linear space translation invariant image degradation model.

are individually extracted. The scatter diagram of luminescence intensity and voltage amplitude is shown in Fig. 14. Due to the flat electrode structure of the EL device, it can be regarded that the central region of the luminescent layer experiences a uniform electric field, and the electric field is linearly related to the applied voltage. Hence, the normalized electric field index is developed based on applied voltage to evaluate the relative electric field. Accordingly, GPR is employed to develop the correlation between the intensity of the G channel and the normalized electric field index. The detailed formulas of GPR can be found in [35].

## *B. Visualization of Electric Field Distribution Under SW Excitation*

In the case of finger electrodes, there are significant electric field enhancement points between the high-voltage electrode, ceramic interface, and composite coating. Therefore, EL initially occurs at the edge of the high-voltage electrode as the voltage increases. As shown in Fig. 15, along the direction of the arrow, the EL intensities appear in areas where the light intensities slowly decay and increase near the HV and GND electrodes, respectively. It can be attributed to the fact that the measured light intensity is formulated by the superposition of the radiation effects of other luminous areas with its own brightness. Therefore, it is necessary to obtain the actual EL intensity to increase the accuracy of the electric field inversion.

For this purpose, the entire measured surface can be divided into *N* finite elements, hence, the actual light intensity at position *i*th can be expressed as

$$\sigma(x,y) = \sum_{m=1}^{M}\sum_{n=1}^{N}\sigma'(x,y)\,h(x-m,y-n) \tag{2}$$

where $\sigma(\cdot,\cdot)$ is the measured light intensity, $h(\cdot,\cdot)$ represents the contribution of the EL intensity at point *j* to the intensity at point *i*, and $\sigma'(\cdot,\cdot)$ denotes the actual luminous intensity. In this study, the EL system for finger electrodes can be treated as the translational invariant system, and the response is independent of the position of the applied excitation. The electric field inversion based on EL intensities can be equivalent to the processes of degradation restoration" model in the field of digital image processing, as shown in Fig. 16. Hence, (2) can be rewritten in the form of convolution based on the property of translation invariance, as follows:

$$\sigma(x,y) = h(x,y) * \sigma'(x,y). \tag{3}$$

To achieve the time domain restoration of degraded images, Richardson [36] developed a Bayesian theory–based algorithm, which applies Poisson distribution and maximum likelihood estimation to achieve an iterative solution of image restoration. Following Bayesian theory, the optimal formula representing the degraded processes is denoted as

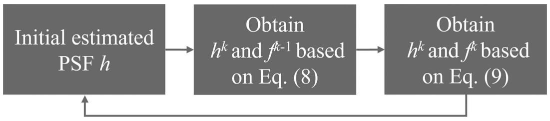

Fig. 17. Schematic diagram of blind deconvolution solution process**.**

$$P(X|Y) = \frac{P(Y|X)\,P(X)}{\int P(Y|X)\,P(X)\,dX} \tag{4}$$

$$\begin{aligned} P(X) &= \int P(X|Y)\,P(Y)\,dY \\ &= \int \frac{P(Y|X)\,P(X)}{\int P(Y|X)\,P(X)\,dX}P(Y)\,dY \\ &= \int \frac{P(Y|X)\,P(Y)}{\int P(Y|X)\,P(X)\,dX}dY\,P(X) \end{aligned} \tag{5}$$

where $X$ denotes the actual image and $Y$ is the degraded one, $P(X)$ represents the grayscale distribution function of the original image as $f(x,y)$, $P(X)$ is the grayscale distribution function of the degraded image as $g(x',y')$, and $P(X|Y)$ represents the PSF of the point $(x,y)$, i.e., $h(x'-x,y'-y)$. Hence, (5) can be rewritten as [36]

$$f(x,y) = \left\{\left[\frac{g(x,y)}{f(x,y) * h(x,y)}\right] * h(-x,-y)\right\} f(x,y) \tag{6}$$

where $*$ denotes convolution operation. Then, the iterative solving can be carried out to estimate the actual image $f(x,y)$ based on the specific degradation image $g(x,y)$ and PSF $h(x,y)$ of the system, exhibited as

$$f_{n+1}(x,y) = \left\{\left[\frac{g(x,y)}{f(x,y) * h(x,y)}\right] * h(-x,-y)\right\} f_n(x,y) \tag{7}$$

where $f_n(x,y)$ and $f_{n+1}(x,y)$ represent the restored images until executing *n* and (*n*+1) iterations, respectively. However, the certain PSF $h(x,y)$ for the EL system investigated in this study is unknown. Hence, the blind deconvolution algorithm based on the above Lucy–Richardson model is further developed to achieve the estimation of $h(x,y)$ and $f(x,y)$. As shown in Fig. 17, there exist two deconvolution steps to estimate PSF and actual image sequentially. It is assumed that the object $f_{n-1}(x,y)$ is known from the (*n*-1)th iteration at the *n*th blind iteration, hence, PSF $h_i^n(x,y)$ can be further evaluated by (8), where *i* is the iteration of (7). Then, $f_i^n(x)$ can be calculated under the same number of Richardson–Lucy iterations [37].

$$h_{i+1}^n(x) = \left\{\left[\frac{g(x)}{h_i^n(x) * f^{n-1}(x)}\right] * f^{n-1}(-x)\right\} h_i^n(x) \tag{8}$$

$$f_{i+1}^n(x) = \left\{\left[\frac{g(x)}{f_i^n(x) * h^n(x)}\right] * h^n(-x)\right\} f_i^n(x). \tag{9}$$

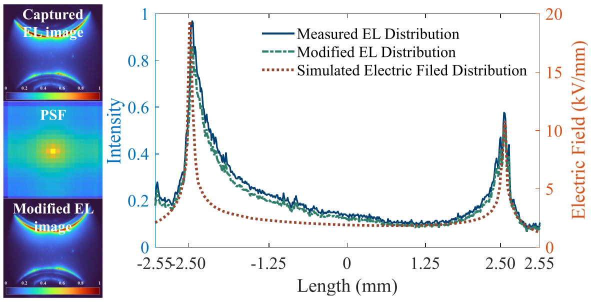

Fig. 18. Blind deconvolution results.

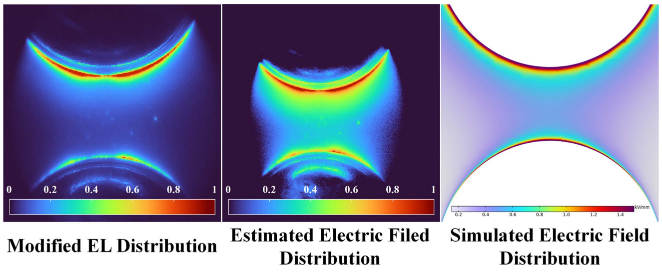

Fig. 19. Comparison between the estimated electric field and the simulated electric field for the finger electrodes.

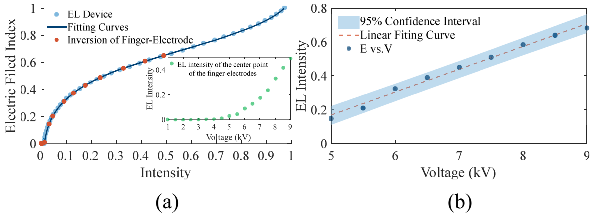

Fig. 20. Inversion results of dimensionless electric field index at the center point of finger-electrode.

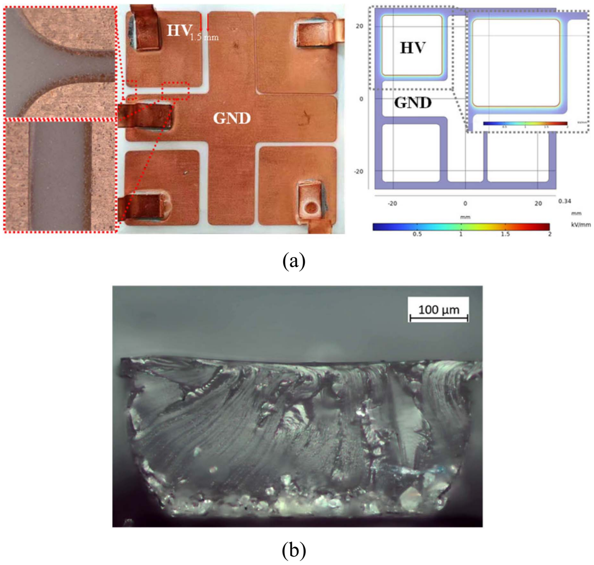

Fig. 21. (a) Schematic diagram of DBC substrate coating composite luminescent material and the simulated electric field results. (b) Schematic diagram of composite luminescent material cross-section between copper layers in DBC substrate.

It is worth noting that the accuracy of the deconvolution result is mainly affected by factors such as the quality of the original image noise, the number of iterations, and the initial PSF. As shown in Fig. 18, the EL distribution of the finger electrodes under SW excitation can be recovered into $h(x, y)$ and $\sigma'(x, y)$. Observing the difference in EL intensity in electrode direction (HV to GND) before and after correction illustrates that the EL intensity to the central area has obvious attenuation after blind deconvolution, which is closer to the simulation results in terms of electric field distribution trend.

Furthermore, the modified EL distribution is applied to derive the corresponding dimensionless electric field index based on the above GPR model, as shown in Fig. 19. Compared with the EL distribution, the inversion results illustrate more advantages in terms of electric field grading visualization. Moreover, based on the consensus that the electric field at the center point of the finger electrode increases linearly with the applied voltage, the effectiveness of the proposed inversion model is verified by evaluating the linearity of the dimensionless electric field index at the center point with increasing applied voltage. As shown in Fig. 20, the EL intensities at the center of the finger-electrode represent an exponential trend with the increase of the applied voltage, which is used to calculate the dimensionless electric field indicators listed as the orange scatters covering the fitting curve. Besides, following the linear fitting results, it can be observed that the dimensionless electric field indexes represent a good linear relationship with the applied voltage, where the goodness of fit achieves 98.85%.

### C. Application to DBC Substrate

To further verify the effectiveness of the electric field inversion approach, the DBC substrate was fabricated as shown in Fig. 21(a). The central cross-shaped copper trace area is grounded, and a high-voltage square electrode with a distance of 1.5 mm from the central grounding electrode is used for model validation. In addition, based on the design criteria for high insulation performance of high-voltage power modules [38], [39], [40], the offset deviation between the upper and lower copper trace edge is set to 0, and the fillet radius of all copper traces is set to 1 mm to achieve optimal electric field homogenization. Then, the trench between the copper trace is coated with the luminescent composite materials, as shown in Fig. 21(a). It can be observed that luminescent powders are uniformly distributed between the trench. To obtain a more intuitive and clear observation of the distribution characteristics of the luminous particles in the cross-section of the coating between the copper layer channels, we completely separated the composite luminescent coating on the surface of the sample using a mechanical stripping method and then characterized the microstructure of the thin film cross-section using the optical microscope (ZEISS Axio scope5), as shown in Fig. 21(b). The results showed that the luminous particles were uniformly distributed on the side of the PDMS matrix close to the ceramic interface. This is attributed to the fact that the luminous particles possess a high specific surface area per unit volume, thereby exhibiting high surface

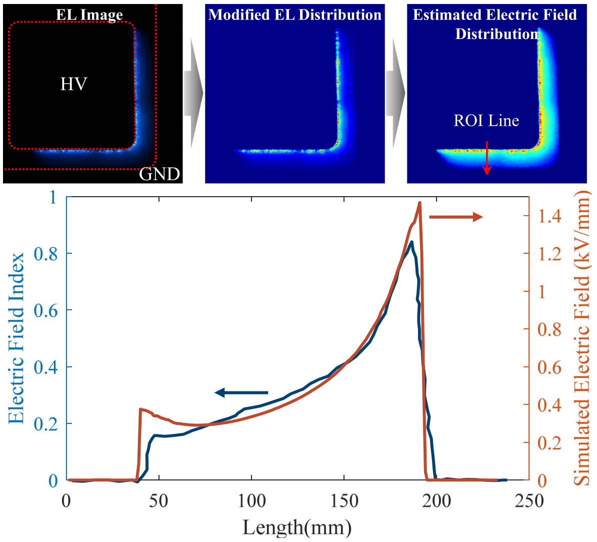

Fig. 22. Comparison between the estimated electric field and the simulated electric field for the DBC substrate.

free energy. When doped into the low-surface-energy polymer matrix PDMS, during the curing process, the particles tend to move towards the bottom of the composite material due to the influence of gravity (the side of the ceramic interface and the side edge of copper layers). Since the composite luminescent coating is applied between the copper layers, the luminescence distribution captured by the digital single-lens reflex camera can be regarded as the result of the combined effect of the electric field in each layer in the vertical direction on the luminescent particles. According to the above-mentioned observation results, the luminescent particles are mainly distributed in the bottom layer of the composite material (near the ceramic interface) and along the edge of the copper layer. Hence, the luminescence distribution mainly characterizes the electric field distribution in its own plane, i.e., the surface of $Al_2O_3$ in this study.

Furthermore, based on the constructed optical detection platform and high-voltage SW generator, the EL distribution of the above specimen is captured under the excitation with frequency of 1 kHz and the p-p value of 0.8 kV, as shown in Fig. 22. Then the corresponding modified EL distribution and estimated dimensionless electric field indexes are derived based on aforementioned inversion procedures. It can be observed that the electric field distribution obtained based on the EL effect approximates the distribution characteristics obtained from finite element simulation results. In addition, by comparing the simulated electric field with the inversion electric field index for the ROI line, it can be found that the inversion results have a similar distribution tendency. However, near the high voltage, the electric field distribution inversion based on the EL effect has a slower electric field rise rate. It can be attributed to the fact that the edge of the copper trace of the actual DBC substrate is grooved (caused by the etching process), and the EL material still produces a certain amount of light on these inclined surfaces. In summary, it can be found that a high-resolution visualization of the high voltage electrode strong field region can be achieved based on the proposed method, which provides an effective technical means for indicating weak insulation points of the DBC substrate.

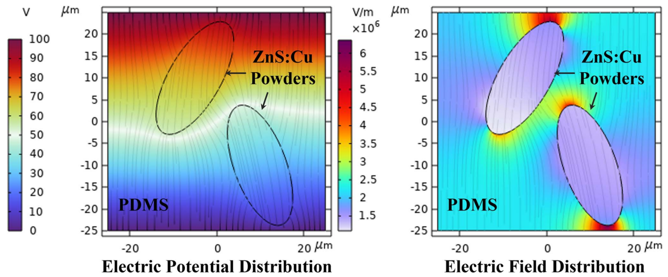

Fig. 23. Diagrams of potential distribution and electric field distribution of the composite EL matrix.

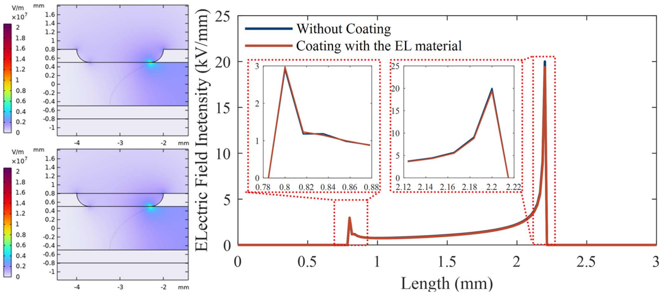

Fig. 24. Effect of coating on the electric field distribution of the DBC substrate.

## V. Discussion

### A. *Effect of EL Coating on Electric Field Distribution of Insulating Structure*

To demonstrate the impact of introducing EL materials on the original electric field distribution, a two-dimensional FEA model is initially established to calculate the potential and electric field distribution, where the ZnS:Cu powders are modeled as ideal ellipses, as shown in Fig. 23. The relative dielectric constant of the ZnS:Cu powders is set as 8.5 [41], and that of PDMS matrix is set to 2.75. Additionally, the driving voltage of 100 V is applied to the upper boundary of the geometry model. The distribution of electric potential and electric field strength are uneven due to the disparate dielectric constants of the ZnS:Cu phosphors and the PDMS matrix. High electric field concentrations are predominantly localized at the top and bottom regions of the spherical ZnS:Cu phosphors. Furthermore, based on the FEA model for the DBC substrates with and without EL coating, it can be found that the thin EL coating essentially has no significant impact on the original electric field distribution, as presented in Fig. 24.

In addition, we conducted a statistical analysis of the PDIV for the samples shown in Fig. 25(a) under the SW excitation, aiming to assess the insulation capabilities of both coated and uncoated samples. As shown in Fig. 25(a), a square electrode featuring a 1.5-mm gap served as the high-voltage electrode. To mimic the actual electric field conditions encountered by the power module, the central cross-section of the upper copper layer, alongside the other square electrodes and the lower copper layer,

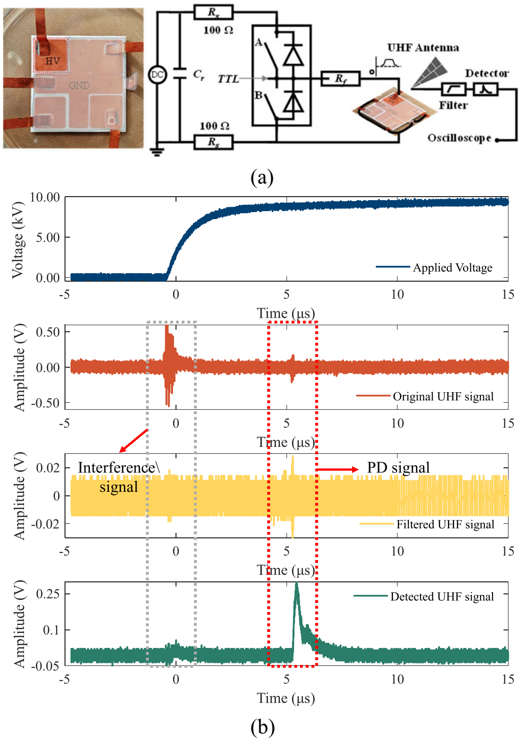

Fig. 25. (a) DBC substrate sample. (b) Comparison of PD signals before and after processing.

is grounded. In accordance with the GB/T 23642-2017 national standard, this paper employs high-frequency electromagnetic measurement techniques to assess PD in the test samples. During the experiment, an ultra-high-frequency (UHF) antenna with a response bandwidth of 50 kHz to 6.5 GHz and a voltage standing wave ratio (VSWR) within the bandwidth of less than 3.0 was used to measure the electromagnetic signals of PD. The experiment utilized a linear envelope detector amplifier with a frequency range of 500–1500 MHz, employing linear envelope detection and a gain of 32 dB. To enhance signal quality, a third-order passive high-pass filter with a cutoff frequency of 500 MHz was installed before the detector, enabling the subsequent linear envelope detector amplifier to process a cleaner signal. This further improved the detection precision and accuracy of PD signals. The comparison of PD signals before and after PD signal processing is shown in Fig. 25(b). To eliminate randomness in the preparation process, 5 samples were set up for each of the two types of experimental objects (DBC substrate samples coated with composite luminescent particles and uncoated ones). Each specimen underwent five independent PDIV measurements under controlled conditions, yielding 25 discrete data points per experimental group. According to IEC 60270 standards, the test voltage is incrementally raised from 1 kV, with increments of 0.2 kV. The interval between each stage is set to 5 s to mitigate interference from transient frequency voltages, and each voltage stage is maintained for 5 min. If no PD event occurs during the current stage, the voltage will increase to the next stage until a PD event is triggered, which is recorded as PDIV. As shown in Fig. 26, the Weibull distribution

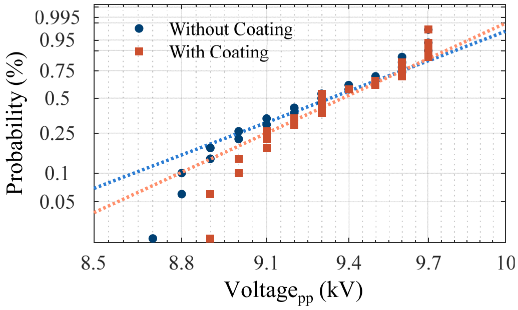

Fig. 26. Weibull distribution of PDIV for the samples with and without coating.

of the PDIV measured for the two cases are similar, where the shape of the scale parameters of the two cases are [9.42, 9.47] and [35.69, 41.64], respectively. It indicates that the coating has no significant effect on the PDIV of the DBC sample, which is consistent with the electric field simulation results.

### *B. Application to the Power Module Substrate*

The proposed method provides *a posteriori* means for electric field distribution and insulation verification of DBC substrates based on the FEA method, which can be regarded as a supplement to the FEA method in real scenarios. Based on the proposed methods, the offline measurement and visualization of the electric field distribution on the power module substrate can be implemented from the following aspects:

*1) Preparation and Coating of Composite Luminescent Materials:* Before the power module is encapsulated with silicone gel, the substrate surface can be initially coated with a composite luminescent material. The detailed preparation process of composite luminescent materials is referred to in Section II-D. Then the composite EL slurry is uniformly coated on the ceramic substrate using a small silicone spatula. Subsequently, the power module is encapsulated with silicone gel based on the standard procedure.

*2) Development of the Optical Inspection Platform:* In this part, a 1-m cubic frame is assembled using aluminum profiles, of which the dual-axis electric slide rail is installed at the top to control the position of the digital camera. Besides, the focal length of the camera is adjusted to the telephoto end to achieve a higher spatial resolution for the inversion of the electric field distribution, and the exposure parameters are set accordingly. Then the slide rail is controlled to position the camera at an optimal distance from the object under test. In addition, the power module is placed in normal operation based on the driver board, and the DC+ terminal is connected to the 2-kV HVdc source. Moreover, the camera is remotely controlled to capture EL images of the power module along a predefined trajectory in the darkroom. Then the images are synchronized in real-time to the host system. The blind deconvolution algorithm is performed to correct the luminescence distribution. Concurrently, the corresponding electric field index of the power module is deduced based on a standard reference inversion model, yielding a detailed map of the electric field distribution under the actual operating conditions of the power module.

*3) Evaluation of Abnormal Electric Field Distribution in Power Module:* Based on the above steps, it is possible to visualize the electric field distribution of the power module over a long time scale. Furthermore, the probabilities of abnormal electric field points are calculated based on the host computer software, and the distribution can be aligned with the original image.

### *C. Applicability Analysis of the Proposed EL Visualization Method Compared With FEA Method*

Traditional methods for simulating electric field distribution, such as the FEA method, often rely on idealized models, such as assuming a uniform and burr-free DBC substrate. However, real-world manufacturing processes introduce microscopic defects like irregular edges and microcracks, which pose challenges for FEA. It struggles with simulating, meshing, and predicting the fine structures at defect interfaces, leading to significant discrepancies between simulated and actual electric field distributions. Additionally, electric field simulation requires handling complex geometric structures and multiphysics field coupling problems, such as electromagnetic–thermal–mechanical coupling, which increases computational demands and necessitates tradeoffs between accuracy and resources. Besides, dielectric parameters of materials under high-frequency excitation, such as conductivity, dielectric constant, and magnetic permeability, are crucial for accurate simulation. And the temperature and frequency dependencies of the above parameters make accurate modeling difficult.

In this study, we developed an electric field visualization method based on the optoelectronic phenomenon of ZnS:Cu. The significance of EL lies in its nondestructive nature, allowing for visualization without physical damage to the material. EL intensity can be used to map the electric field distribution within insulating materials without causing any physical damage. This is especially useful for inspecting the integrity of high-voltage components and identifying potential hotspots or regions of high electric field stress. In the insulation design and manufacturing process of power modules, EL-based technology can be used to visualize the electric field distribution on the substrate and further guide the optimization design of insulation structures.

Furthermore, the insulation verification for the pre-designed specimen plays an important role in the overall insulation evaluation of the power module. Currently, in response to the actual operating conditions of power modules, there is a need for more accurate and effective methods to verify the insulation performance. The detection of PD starting voltage under high-voltage high-frequency SW excitation has problems such as low detection rate of pulse signals (especially in high-frequency noise environments) and easy submergence of weak discharge signals, resulting in a high risk of missed detection of insulation defects. At the same time, existing evaluation methods lack a quantitative correlation model between discharge patterns and insulation hazard, making it difficult to achieve accurate mapping from discharge characteristics to remaining life prediction. In contrast, the proposed method can be used to identify high electric field stress areas that may cause the malfunction. The real-time monitoring of electric field distribution and the integrated spectral distribution can be achieved by integrating the optical sensors into the devices. It enables early detection of potential issues such as abnormal electric field stress or insulation degradation and allows for proactive maintenance to prevent equipment failure. Hence, the proposed method offers *a posteriori* approach for analyzing the electric field distribution and verifying the insulation of the DBC substrate, which serves as a supplement to the traditional FEA method.

It is also important to highlight that the luminescence characteristics exhibit typical temperature and frequency dependencies. Further exploration is essential to assess the effectiveness of EL methods in addressing multiphysical field coupling issues, such as electromagnetic-thermal-mechanical coupling. Meanwhile, by integrating the deep learning model with spatiotemporal prediction techniques, a dynamic model that couples multiple physical fields can be developed. It will enable rapid inversion under complex operating conditions, thus significantly enhancing the applicability of the proposed method. Furthermore, it is imperative to extend this method to emerging wide-bandgap semiconductor devices and 3-D packaging modules, which exhibit intensified electric field complexities due to miniaturized geometries, high-frequency switching, and heterogeneous material interfaces, demanding refined spatial resolution and adaptive calibration frameworks. Moreover, future research will integrate industrial feasibility requirements to explore optimization pathways for the preparation processes of composite luminescent materials. In-depth investigations will be conducted on the compatibility between EL particles and widely used encapsulation materials (e.g., silicone gel, epoxy resin), to establish a material compatibility database to provide robust data support for practical applications.

## VI. CONCLUSION

Focusing on insulation verification for the DBC substrate of a high-voltage power module under high-voltage SW excitation, a visual electric field inversion method for the abnormal shape electrodes was established based on the EL effect. First, the composite luminescent materials with different doping ratios were prepared, and the dielectric properties were evaluated to determine the optimal doping ratio. Furthermore, the EL mechanism and the high-frequency dependence of EL under SW excitation were revealed based on the temporal resolution photoresponse and integral spectral characteristics. Then, the mapping relationship between the g-channel color scale intensity of EL devices and the dimensionless electric field index is established based on the GPR model, treating it as a standard electric field inversion model. Further considering the typical structure of copper-clad laminate of the power module, the finger electrode was prepared, and the physical process of El and corona discharge was determined. Considering that the actual measured light intensity is the superposition of the radiation effect of other luminous regions and its own brightness, a blind deconvolution algorithm is proposed to correct the luminous distribution of the finger electrode. Meanwhile, the dimensionless electric field index distribution is obtained based on the standard inversion model. Besides, the effectiveness of the proposed inversion algorithm is verified by evaluating the linearity of the electric field index at the center of the finger electrode. In addition, the above electric field inversion method is applied to a physical DBC substrate. The experimental results show that the proposed method achieves high-resolution electric field visualization and visualizes abnormal electric field regions. In summary, it can be concluded that this study can provide novel guidance for the visualization and quantitative evaluation of abnormal electric field distribution of DBC substrate.

## REFERENCES

[1] A. Anurag, S. Acharya, S. Bhattacharya, T. R. Weatherford, and A. A. Parker, "A gen-3 10-kV SiC MOSFET-based medium-voltage three-phase dual active bridge converter enabling a mobile utility support equipment solid State transformer," *IEEE J. Emerg. Sel. Topics Power Electron.*, vol. 10, no. 2, pp. 1519–1536, Apr. 2022, doi: 10.1109/JESTPE.2021.3069810.

[2] H. Lee, V. Smet, and R. Tummala, "A review of SiC power module packaging technologies: Challenges, advances, and emerging issues," *IEEE J. Emerg. Sel. Topics Power Electron.*, vol. 8, no. 1, pp. 239–255, Mar. 2020, doi: 10.1109/JESTPE.2019.2951801.

[3] Z. Zhang et al., "Packaging of a 10-kV double-side cooled silicon carbide diode module with thin substrates coated by a nonlinear resistive polymer-nanoparticle composite," *IEEE Trans. Power Electron.*, vol. 37, no. 12, pp. 14462–14470, Dec. 2022, doi: 10.1109/TPEL.2022.3190303.

[4] M. M. Tousi and M. Ghassemi, "Electrical insulation design and accurate estimation of temperature via an electrothermal model for a 10 kV SiC power module packaging," in *Proc. IEEE Conf. Electr. Insul. Dielectr. Phenom.*, 2020, pp. 407–410, doi: 10.1109/CEIDP49254.2020.9437513.

[5] C. DiMarino et al., "Design and experimental validation of a wire-bond-less 10-kV SiC MOSFET power module," *IEEE J. Emerg. Sel. Topics Power Electron.*, vol. 8, no. 1, pp. 381–394, Mar. 2020, doi: 10.1109/JESTPE.2019.2944138.

[6] Y. Wang et al., "Space-charge accumulation and its impact on high-voltage power module partial discharge under dc and PWM waves: Testing and modeling," *IEEE Trans. Power Electron.*, vol. 36, no. 10, pp. 11097–11108, Oct. 2021, doi: 10.1109/TPEL.2021.3072655.

[7] A. Cavallini, D. Fabiani, and G. C. Montanari, "Power electronics and electrical insulation systems - Part 1: Phenomenology overview," *IEEE Elect. Insul. Mag.*, vol. 26, no. 3, pp. 7–15, May/Jun. 2010, doi: 10.1109/mei.2010.5482783.

[8] J.-H. Fabian, S. Hartmann, and A. Hamidi, "Analysis of insulation failure modes in high power IGBT modules," in *Proc. 48th IAS Annu. Meeting. Conf. Rec. Ind. Appl. Conf.*, 2005, vol. 2, pp. 799–805, doi: 10.1109/IAS.2005.1518425.

[9] X. Liu et al., "Characteristics and identification of partial discharge for insulation structures in high voltage IGBT modules under positive square wave voltage," *IEEE Trans. Power Electron.*, vol. 38, no. 4, pp. 5347–5359, Apr. 2023, doi: 10.1109/TPEL.2022.3232327.

[10] T. Ebke, A. Khaddour, and D. Peier, "Degradation of silicone gel by partial discharges due to different defects," in *Proc. 8th Int. Conf. Dielectr. Mater., Meas. Appl.*, 2000, pp. 202–207, doi: 10.1049/cp:20000505.

[11] S. Mo et al., "Analysis of discharge caused by soldering defect in wire-bonding power module," *IEEE Trans. Compon., Packag. Manuf. Technol.*, vol. 12, no. 12, pp. 1907–1913, Dec. 2022, doi: 10.1109/TCPMT.2022.3227324.

[12] J. Schulz-Harder, "Advantages and new development of direct bonded copper substrates," *Microelectron. Rel.*, vol. 43, no. 3, pp. 359–365, Mar. 2003, doi: 10.1016/S0026-2714(02)00343-8.

[13] B. Passmore et al., "The next generation of high voltage (10 kV) silicon carbide power modules," in *Proc. IEEE 4th Workshop Wide Bandgap Power Devices Appl.*, 2016, pp. 1–4, doi: 10.1109/WiPDA.2016.7799900.

[14] U. Mehrotra, A. J. Morgan, and D. C. Hopkins, "Design and characterization of 3.3 kV-15 kV rated DBC power modules for developmental testing of WBG devices," in *Proc. IEEE Appl. Power Electron. Conf. Expo.*, 2021, pp. 2351–2356, doi: 10.1109/APEC42165.2021.9487311.

[15] C. M. DiMarino, B. Mouawad, C. M. Johnson, D. Boroyevich, and R. Burgos, "10-kV SiC MOSFET power module with reduced common-mode noise and electric field," *IEEE Trans. Power Electron.*, vol. 35, no. 6, pp. 6050–6060, Jun. 2020, doi: 10.1109/TPEL.2019.2952633.

[16] X. Li et al., "EMI mitigation with stacking DBC substrate for high voltage power module," in *Proc. IEEE Energy Convers. Congr. Expo.*, 2022, pp. 1–7, doi: 10.1109/ECCE50734.2022.9947391.

[17] J. Li, Y. Liang, Y. Mei, X. Tang, and G.-Q. Lu, "Packaging design of 15 kV SiC power devices with high-voltage encapsulation," *IEEE Trans. Dielectr. Electr. Insul.*, vol. 29, no. 1, pp. 47–53, Feb. 2022, doi: 10.1109/TDEI.2022.3146569.

[18] X. Chen, Q. Wang, N. Ren, C. Dai, M. Awais, and A. Paramane, "Potential of epoxy nanocomposites for packaging materials of high voltage power modules: A validation using experiments and simulation," *IEEE Trans. Dielectr. Electr. Insul.*, vol. 28, no. 6, pp. 2161–2169, Dec. 2021, doi: 10.1109/TDEI.2021.009778.

[19] Y. Lin et al., "Temperature- and degradation-dependent maximum electric field stress in wire-bonding power modules under PWM waves," *IEEE J. Emerg. Sel. Topics Power Electron.*, vol. 10, no. 6, pp. 7653–7664, Dec. 2022, doi: 10.1109/JESTPE.2022.3195177.

[20] G. Wijeweera, B. Bahreyni, C. Shafai, A. Rajapakse, and D. R. Swatek, "Micromachined electric-field sensor to measure ac and dc fields in power systems," *IEEE Trans. Power Del.*, vol. 24, no. 3, pp. 988–995, Jul. 2009, doi: 10.1109/TPWRD.2008.2008427.

[21] Q. Yang, S. Sun, Y. He, and R. Han, "Intense electric-field optical sensor for broad temperature-range applications based on a piecewise transfer function," *IEEE Trans. Ind. Electron.*, vol. 66, no. 2, pp. 1648–1656, Feb. 2019, doi: 10.1109/TIE.2018.2831170.

[22] M. Yazdani, D. J. Thomson, and B. Kordi, "Passive wireless sensor for measuring ac electric field in the vicinity of high-voltage apparatus," *IEEE Trans. Ind. Electron.*, vol. 63, no. 7, pp. 4432–4441, Jul. 2016, doi: 10.1109/TIE.2016.2546845.

[23] Z. Li, H. Yuan, Y. Cui, Z. Ding, and L. Zhao, "Measurement of distorted power-frequency electric field with integrated optical sensor," *IEEE Trans. Instrum. Meas.*, vol. 68, no. 4, pp. 1132–1139, Apr. 2019, doi: 10.1109/TIM.2018.2864019.

[24] X. Yang, Y. Jia, L. Gao, S. Ji, and Z. Li, "A method for measuring surface electric field intensity of insulators based on electroluminescent effect," *Energy Rep.*, vol. 6, pp. 1537–1543, Dec. 2020, doi: 10.1016/j.egyr.2020.10.056.

[25] T. Chen, C. Shafai, A. Rajapakse, J. S. H. Liyanage, and T. D. Neusitzer, "Micromachined ac/dc electric field sensor with modulated sensitivity," *Sensors Actuators A, Phys.*, vol. 245, pp. 76–84, Jul. 2016, doi: 10.1016/j.sna.2016.04.054.

[26] M. PourhosseiniAsl et al., "Magnetic-force-induced-luminescent effect in flexible ZnS:Cu/PDMS/NdFeB composite," *Adv. Mater. Interfaces*, vol. 10, no. 9, 2023, Art. no. 2202332, doi: 10.1002/admi.202202332.

[27] J. Liao et al., "Self-powered, flexible, and instantly dynamic multicolor electroluminescence device with bi-emissive layers for optical communication," *Nano Energy*, vol. 112, Jul. 2023, Art. no. 108488, doi: 10.1016/j.nanoen.2023.108488.

[28] X.-B. Guo et al., "Self-diagnosis and high-flashover-strength electroluminescence coatings," *IEEE Trans. Dielectr. Electr. Insul.*, vol. 29, no. 2, pp. 663–671, Apr. 2022, doi: 10.1109/TDEI.2022.3157896.

[29] T. Wen, X. Cui, X. Li, H. Ma, and Z. Zhao, "Time-domain finite element method for transient electric field and transient charge density on dielectric interface," *CSEE J. Power Energy Syst.*, vol. 8, no. 1, pp. 143–154, Jan. 2022, doi: 10.17775/CSEEJPES.2020.02170.

[30] M. Samet, A. Kallel, and A. Serghei, "Maxwell–Wagner-Sillars interfacial polarization in dielectric spectra of composite materials: Scaling laws and applications," *J. Composite Mater.*, vol. 56, no. 20, pp. 3197–3217, Aug. 2022, doi: 10.1177/00219983221090629.

[31] F. Yang et al., "Interleaved planar packaging method of multichip SiC power module for thermal and electrical performance improvement," *IEEE Trans. Power Electron.*, vol. 37, no. 2, pp. 1615–1629, Feb. 2022, doi: 10.1109/TPEL.2021.3106316.

[32] P. Ning, Z. Liang, and F. Wang, "Power module and cooling system thermal performance evaluation for HEV application," *IEEE J. Emerg. Sel. Topics Power Electron.*, vol. 2, no. 3, pp. 487–495, Sep. 2014, doi: 10.1109/JESTPE.2014.2303143.

[33] R. V. Kuznetsova, "Nature of the surface barriers in ZnS electroluminophors," *J. Appl. Spectrosc.*, vol. 27, no. 2, pp. 1068–1070, Aug. 1977, doi: 10.1007/BF00609501.

[34] R. Polícia, D. M. Correia, N. Peřinka, C. R. Tubio, and S. Lanceros-Méndez, "Influence of polymer matrix on the luminescence of phosphor based printable electroluminescent materials and devices," *Polymer*, vol. 268, Feb. 2023, Art. no. 125700, doi: 10.1016/j.polymer.2023.125700.

[35] C. E. Rasmussen and C. K. I. Williams, *Gaussian Processes for Machine Learning*. Cambridge, MA, USA: MIT Press, 2005, doi: 10.7551/mit-press/3206.001.0001.

[36] W. H. Richardson, “Bayesian-based iterative method of image restoration∗,” *J. Opt. Soc. Amer.*, vol. 62, no. 1, pp. 55–59, Jan. 1972, doi: 10.1364/JOSA.62.000055.

[37] D. A. Fish, J. G. Walker, A. M. Brinicombe, and E. R. Pike, “Blind deconvolution by means of the Richardson–Lucy algorithm,” *J. Opt. Soc. Amer. A*, vol. 12, no. 1, pp. 58–65, Jan. 1995, doi: 10.1364/JOSAA.12.000058.

[38] C. F. Bayer, U. Waltrich, A. Soueidan, E. Baer, and A. Schletz, “Partial discharges in ceramic substrates - correlation of electric field strength simulations with phase resolved partial discharge measurements,” in *Proc. Int. Conf. Electron. Packag.*, 2016, pp. 530–535, doi: 10.1109/ICEP.2016.7486884.

[39] L. Wang, Z. Zeng, P. Sun, S. Ai, J. Zhang, and Y. Wang, “Electric-field-dominated partial discharge in medium voltage SiC power module packaging: Model, mechanism, reshaping, and assessment,” *IEEE Trans. Power Electron.*, vol. 37, no. 5, pp. 5422–5432, May 2022, doi: 10.1109/TPEL.2021.3132695.

[40] M. M. Tousi and M. Ghassemi, “Characterization of nonlinear field-dependent conductivity layer coupled with protruding substrate to address high electric field issue within high-voltage high-density wide bandgap power modules,” *IEEE J. Emerg. Sel. Topics Power Electron.*, vol. 8, no. 1, pp. 343–350, Mar. 2020, doi: 10.1109/JESTPE.2019.2953145.

[41] C. H. Yang, B. Chen, J. Zhou, Y. M. Chen, and Z. Suo, “Electroluminescence of giant stretchability,” *Adv. Mater.*, vol. 28, no. 22, pp. 4480–4484, Jun. 2016, doi: 10.1002/adma.201504031.

**Kai Wang** was born in Hubei Province. China, in 1992. He received the M.S. degree in electrical engineering from China Three Gorges University, Yichang, China, in 2021. He is currently working toward the Ph.D. degree in high voltage technology from Xi’an Jiaotong University, Xi’an, China.

His research interests include power module packaging insulation, partial discharge detection and diagnosis, and layout insulation verification.

**Donglei Dai** received the B.S. degree in electrical engineering and automation from East China Jiaotong University, Nanchang, China, in 2018, and the M.S. degree in electrical engineering from Southwest Jiaotong University, Chengdu, China, in 2021. He is currently working toward the Ph.D. degree in electrical engineering with Xi’an Jiaotong University, Xi’an, China.

His research interests include reliability and visualization evaluation methods of packaging insulation for high-voltage power modules.

**Chongxing Zhang** received the B.S. and Ph.D. degrees in electrical engineering from Xi’an Jiaotong University, Xi’an, China, in 2013 and 2025, respectively.

He is currently specializing in smart situation awareness technology for power equipment and insulation design and assessment for power electronic converters. His research interests include high-voltage engineering gaseous discharge, partial discharge detection and diagnosis, and insulation status assessment of power equipment.

**Ming Dong** (Member, IEEE) was born in Shaanxi, China, in 1978. He received the B.S. and Ph.D. degrees in electrical engineering from Xi’an Jiaotong University, Xi’an, China, in 2001 and 2006, respectively.

He is currently a Professor with the High Voltage Technology Institute, School of Electrical Engineering, Xi’an Jiaotong University. His current research interests include the aging mechanism of dielectric material and his research work is intelligent HV equipment and power condition assessment.

**Ming Ren** (Member, IEEE) was born in Shaanxi, China, in 1987. He received the B.S. and Ph.D. degrees in electrical engineering from Xi’an Jiaotong University, Xi’an, China, in 2009 and 2013, respectively.

In May 2014, he joined Xi’an Jiaotong University, as a Lecturer, where he is currently a Professor with the High Voltage Technology Institute, School of Electrical Engineering. His current research interests include high-voltage engineering and his present research works are risk assessment of UHV/EHV power equipment, insulation status diagnosis, and advanced fault detection and protection technologies for power systems.